Materials & Design 227 (2023) 111759

Contents lists available at ScienceDirect

Materials & Design

journal homepage: www.elsevier.com/locate/matdes

Gaussian distribution-based modeling of cutting depth predictions of kerf profiles for ductile materials machined by abrasive waterjet

Jianfeng Chen [a], Yemin Yuan [a], Hang Gao [a,*], Tianyi Zhou [a,b]

[a] School of Mechanical Engineering, Dalian University of Technology, Dalian 116024, China
[b] AVIC Shenyang Aircraft Design & Research Institute, Shenyang, 110035, China

HIGHLIGHTS

- The cutting depth of a kerf profile following the Gaussian distribution was developed.
- The energy distribution of the jet was analyzed by applying the first-order derivation.
- The profile fitting of the extracted kerf was performed using a step-by-step approximation method.
- The stepwise approximation of the tangent profiles corresponded strongly to the predicted profiles.
- An important basis for abrasive waterjet machining was provided.

GRAPHICAL ABSTRACT

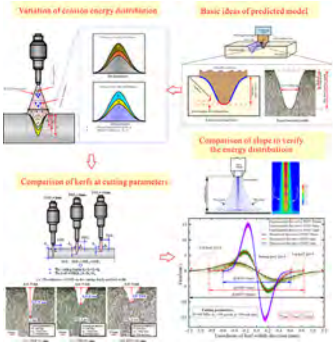

ARTICLE INFO

Article history:
Received 5 November 2022
Revised 31 January 2023
Accepted 15 February 2023
Available online 18 February 2023

Keywords:
Abrasive waterjet
Cutting depth prediction
Gaussian distribution
Ductile materials

ABSTRACT

This study proposes a model for the erosion cutting profile to predict the cutting depth under different process parameters for abrasive waterjet (AWJ) cutting. The model follows the Gaussian distribution and is experimentally validated. Additionally, the effects of the dimensional characteristics and process parameters on the kerf geometry were analyzed. It was found that the water pressure, abrasive flow rate, and focusing tube traverse speed changed the slope of the kerf wall without changing the kerf width. However, the standoff distance (SOD) changes the kerf width, whereas the slope of the kerf wall induces minor changes. Furthermore, based on the first-order derivation of the extracted kerf profile, the relationship between jet energy, cutting depth, and kerf width was analyzed. The experimental results revealed that: 1) the relationship between the reduction in the jet energy distribution and cutting depth is non-linear; 2) the jet energy distribution is smallest at the kerf top edge and bottom section. The predictive cutting depth model and jet energy distribution will enable the subsequent optimization of process parameters in the AWJ process.

1. Introduction

Since its inception as an emerging versatile and cool-machine processing technology, abrasive waterjet (AWJ) machining has been acclaimed for its extraordinary advantages over traditional machining technologies and holds great promise for the next generation of low-cost [1], high-efficiency [2], and pollution-free processing technologies [3]. However, the cutting depth and energy distribution are high-precision machining parameters in AWJ. For practical applications, controllable and precise cutting depths are a topic of great interest.

The cutting depth model has been widely studied by several researchers from various perspectives. Previous research exploring

---

* Corresponding author.
E-mail address: ghangdlut@126.com (H. Gao).

https://doi.org/10.1016/j.matdes.2023.111759
0264-1275/

Nomenclature

α	Angle of erosion [°]
α_0	Angle of erosion for erosion peak [°]
α_t	Angle of erosion at top of kerf [°]
ρ_p	Density of particle [g/cm^3]
ρ_w	Density of water [g/cm^3]
μ	The focusing tube traverse speed [mm/min]
τ	Momentum transfer efficiency [-]
σ_f	Material flow stress [MPa]
C	Fraction to take into account when the cutting wear is terminated with only partial reference to the total jet diameter [-]
d_0	Orifice diameter [mm]
d_f	The corresponding kerf width at half the cutting depth [mm]
d_j	The jet diameter [mm]
d_w	The kerf width [mm]
h	Any cutting depth [mm]
h_e	The effective cutting depth [mm]
H	The limit cutting depth [mm]
k	Set the slope value of the kerf profile to reflect the effective cutting depth requirement [-]
m_a	Abrasive flow rate [g/min]
P	Water pressure [MPa]
R_f	Roundness factor of particles [-]
SOD	Standoff distance [mm]
w	Standard deviation [-]
v_0	The velocity of high-speed water jet formation from high-pressure water [mm/min]
v_c	A characteristic erosion velocity of abrasive [mm/min]
δV	The material removal rate [mm^3/min]

erosive processes adopted a mathematical model using the erosion model and impact damage to develop the maximum cutting depth [4]. Huang et al. [5] developed a modified erosion model using kinematic jet-solid penetration to predict the cutting depth based on different erosion methods along the kerf. Paul et al. [6] introduced the concept of a generalized kerf shape by AWJ to develop the total cutting depth, which considers the along-kerf width and increasing cutting depth. Mohankumar et al. [7] used modified process parameters to attain the peak cutting depth and develop a semi-empirical equation using Buckingham's theorem. Niranjan et al. [8] experimentally and systematically determined the cutting depth using a profile projector to investigate the effects of process parameters. Ketan et al. [9] experimented with an AA2014 alloy to establish a predictive cutting depth using a fuzzy-logic technique. Recently, surface roughness and cutting depth have also been studied. Ozcelik et al. [10] used different cutting parameters to develop a cuttability abacus to predict the cutting depth and surface roughness. Aydin et al. [11] investigated the machinability of granite to relate the cutting depth to the cutting wear zone using a Taguchi orthogonal array. Nie et al. [12] studied the effect of different water pressures on the cutting depth to analyze the topographic characteristics and formation mechanisms of the cut faces. Yuvaraj et al. [13] used the variation in the erosion angle to analyze its effect on the cutting depth and machining quality. Aydin et al. [14] conducted an experimental investigation to evaluate the cutting process, cutting depth, surface roughness, and kerf angle of granite.

In recent years, mathematical models of kerf profiles have been developed by several researchers. Feng et al. [15] assumed a cosine function for the kerf profile in a single-pass milling. Laurinat et al. used a modified cosine function to analyze different kerf profiles, compared the experimental and theoretical profiles, and established a law for the kerf profile between the focusing tube speed and standoff distance. Valíček et al. [17] used the projection method of the rotation plane and the normal vector to analyze the different stages of material removal to understand the material removal mechanism of AWJ machining under varying surface topographies.

Paul et al. [18] used the difference in machining surface quality to divide the kerf profile into two regions, and then modeled the different cutting depths based on the profile characteristics of different machining regions and variations in the jet flow for a ductile material. Aiming at the material removal of the jet structure, Hlaváč [19] used the theoretically determined physical interrelations between the parameters and characteristics of an AWJ to determine the striation model of material properties, cutting depth, and cutting parameters to compensate for the negative effects of jet retardation inside the kerf and suppression of striations on the kerf walls. Srinivasu et al. [20] analyzed the effects of the tilting angle and traverse feed of the focusing tube on geometric and dimensional kerf variations. The profile produced by the kerf converts the cosine function into a more elliptical shape by varying the tilting angle of the nozzle. Hlaváč et al. [21,22] adopted the difference between the top and bottom kerf widths and the angle between the tangent to the striation curve and impinging jet axis to compensate for the characteristic phenomenon of AWJ cutting, which is aimed at eliminating the defects of jet erosion. Theoretically, a change in the erosion geometry is achieved by changing the local impact angle of the jet, thus enabling the machining of complex surfaces, and the variation in the kerf slope is analyzed by the jet plume [23].

According to the literature above, predictive models for cutting depth have been extensively studied under the erosion process and cutting parameters. However, studies associated with the qualitative model of kerf shape in the erosion process by the AWJ are limited. In addition, the hypothesis that the micro-cutting erosion model is approximate to the erosion profile has rarely been explored. This is because the jet energy dissipates as the cutting depth increases and the machined quality deteriorates.

In this study, a Gaussian distribution profile was assumed by the kerf width for any cutting depth in micro-cutting, material removal of micro-cutting, and kinematic jet-solid penetration along the variation in kerf width. In addition, the effects of the process parameters on the kerf geometry and its dimensional characteristics during the AWJ process were analyzed. Furthermore, to clarify the change in the erosion profile, the slope of the kerf profile based on the first-order derivative was analyzed by numerical extraction of the kerf profile. Additionally, a cutting depth model based on jet energy variation was proposed so that the cutting depth could be guaranteed based on different processing quality requirements. Finally, the predictive model was verified and found to correlate well with experimental values.

The predictive model for cutting depth was studied based on a Gaussian distribution, with particular emphasis on the distribution of jet energy. To achieve this scope, the following aspects were investigated: Section 2 introduces the theoretical model of cutting depth and the first-order partial derivative model based on the Gaussian distribution of the kerf profile; In Section 3, three ductile material properties (Section 3.1), image processing and kerf profile extraction (Section 3.2) are introduced in detail; In Section 4, the verification of the cutting depth model with Gaussian distribution (Section 4.1) and analysis of the jet energy distribution and its process parameters on the energy variation (Section 4.2) are presented; Section 5 summarizes the cutting depth model and its energy distribution.

2. Analytical approach

In AWJ machining, different kerf shapes reflect the machining capacity of different material removals under different machining conditions. Therefore, it is helpful to divide the cutting depth into different machining areas by analyzing the erosion profile. As the cutting depth increases, the jet becomes unstable and is easily deflected at the bottom. This process cannot fully guarantee penetration of the workpiece and causes secondary erosion damage to the bottom contour. A model based on the geometry of the erosion kerf and the process parameters was established to optimize the cutting depth during the jet machining of a workpiece..

Hlaváč et al. [24] used hydrodynamics and unconventional views on liquid jet formation inside the nozzle to determine the velocity profile. Based on the geometry of the kerf during impact, various profiles of the kerf are assumed to have a Gaussian distribution in the micro-cutting process, as shown in Fig. 1.

$$h = H \cdot e^{-\frac{d_w^2}{2w^2}} \tag{1}$$

where h, H, and d_w represent the cutting depth, cutting-depth limit, and kerf width. d_f represents the corresponding kerf width at half the cutting depth, and $w = \frac{d_f}{\sqrt{\ln 4}}$ represents the standard deviation.

The variation in the kerf width based on the Gaussian distribution was similar to that of the kerf, whereas the variation in the cutting depth profile was similar to that of the Gaussian distribution width. Therefore, the relationship between the kerf width d_w and cutting depth h can be expressed as follows:

$$d_w = \frac{2d_f\sqrt{\ln H - \ln h}}{\sqrt{\ln 2}} \tag{2}$$

In steady micro-cutting, the material removal rate is deduced using the geometrically determined displacement, as follows [25]:

$$\delta V = \delta h \cdot d_w \cdot u \tag{3}$$

where u represents the focusing tube traverse speed.

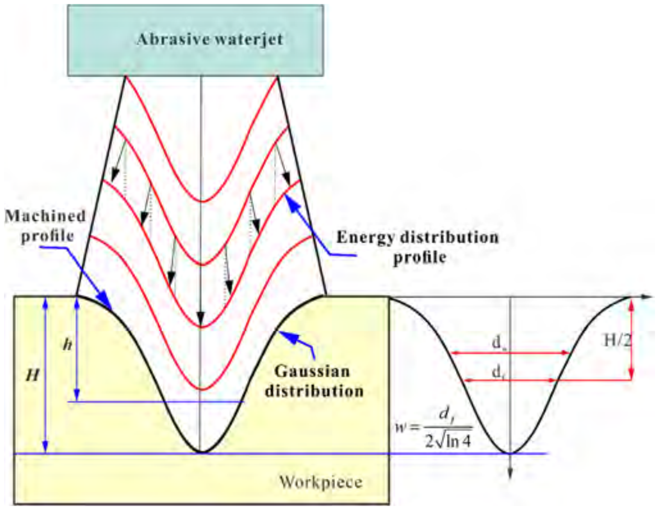

Fig. 1. Typical kerf geometry for ductile materials.

Hashish [26] used the Finnie micro-machining model to establish a material removal model for impact abrasives with small impact angles.

$$\delta V = \frac{7}{\pi} \cdot \left[\frac{R_f^{3/5} \cdot d_j \cdot m_a}{\rho_P}\right] \cdot \left[\frac{v_0}{v_C}\right]^{2.5} \cdot \sin 2\alpha \cdot \sqrt{\sin\alpha} \tag{4}$$

where v_0 represents the velocity from the high-pressure pump through the sapphire tiny aperture, determined by $v_0 = \tau \cdot \sqrt{\frac{2 \cdot P}{\rho_W}}$; v_C represents the characteristic erosion velocity of the abrasive, determined using $v_C = \sqrt{\frac{3 \cdot \sigma_f \cdot R_f^{3/5}}{\rho_p}}$; d_j represents the jet diameter, determined using $d_j = 0.24 \cdot d_0 \cdot \sqrt{SOD}$; $R_f^{3/5}$ represents the roundness factor of the particles.

Material removal by the jet is the accumulated result of erosion by a large number of abrasive particles in the jet. To obtain the jet removal material erosion rate, the calculation was performed by the material removal of single particles[27]:

$$\delta V = \frac{14 \cdot C \cdot m_a}{\pi \cdot \rho_P \cdot \alpha_t} \cdot \left[\frac{v_0}{v_C}\right]^{2.5} \cdot \alpha^{1.5} \tag{5}$$

where α represents the angle of impact. C is given by $C = (1 - \frac{\alpha_t}{\alpha_0})$, where α_0 and α_t represent the angle of the maximum erosion rate and erosion angle at the top of the kerf determined using $\alpha_t = \frac{1}{(\frac{14 \cdot m_a}{\pi \cdot \rho_p \cdot d_w^2 \cdot \mu})^{2.5}(\frac{v_0}{v_C})}$, respectively.

When the erosion process of the jet is in the steady-state phase, the calculation based on the overall material removal rate with an abrasive is theoretically obtained in agreement with the geometric aspect of the calculated displacement rate:

$$dh \cdot u \cdot \left[2\sqrt{2} \cdot d_w \cdot \sqrt{\ln H - \ln h}\right] = \frac{14 \cdot C \cdot m_a}{\pi \cdot \rho_P \cdot \alpha_t} \cdot \left[\frac{v_0}{v_C}\right]^{2.5} \cdot \alpha^{1.5} \tag{6}$$

where the cutting depth, $h = 0$, the jet velocity $v_0 = 0$.

From Eq. (6), the erosion rate evaluated according to jet physics is equal to the geometric erosion, which can be obtained using the following formula to obtain the limit cutting depth:

$$\int_0^H dh \cdot u \cdot \left[2\sqrt{2}d_w \cdot \sqrt{\ln H - \ln h}\right] = -(\frac{14}{\pi}) \cdot \frac{\dot{m} \cdot C}{\rho_p \cdot \alpha_t \cdot} (\frac{v_0}{v_c})^{2.5} \int_{\alpha_t}^{0} \alpha^{1.5} d\alpha \tag{7}$$

Thus, the limit cutting depth can be expressed as:

$$H = \frac{28}{\sqrt{2}\pi^2} \cdot \frac{m_a \cdot C}{\rho_a \cdot \mu \cdot \frac{0.24 \cdot d_0 \cdot \sqrt{SOD}}{2 \cdot \ln 4}} \cdot \left[\frac{\sqrt{2P/\rho_w}}{\frac{3 \cdot \sigma \cdot R_f^{0.6}}{\rho_a}}\right]^{2.5} \cdot \alpha_t^{1.5} \tag{8}$$

Table 1
Material properties of Aluminum alloy 6061 and 304 stainless steel and Ti-6Al-4 V [28–30].

Material type	Aluminum alloy 6061	304 stainless steel	Ti-6Al-4 V
Vickers hardness (H_v)	95	241	330
Yield Stress (MPa)	276	275	883
Ultimate tensile stress (MPa)	310	585	1035
Density (g/cm^3)	2.7	7.92	4.43
Chemical composition	Al 98% Mg 0.9–1.3% Si 0.5–0.9%	Si 1.0% C 0.09% Cr 18–21% Ni 8.0–10.6%	Ti 90% Al 5.5–6.8% V 3.5–4.5%

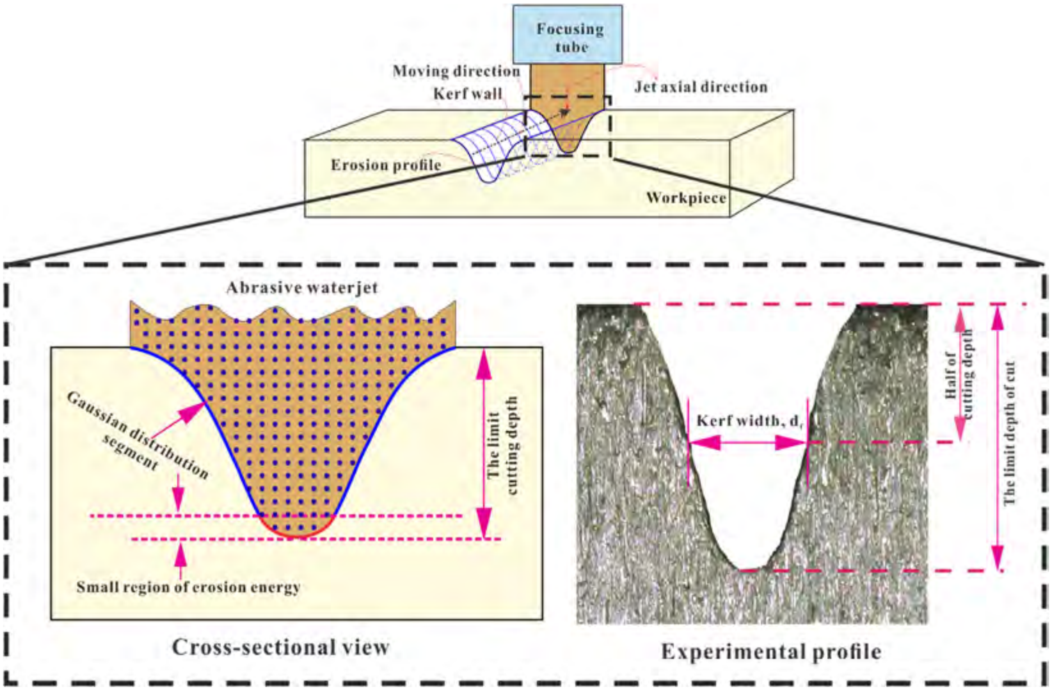

Fig. 2. Experimental setup.

Table 2
The machining process and its detailed values.

	Value
Pressure inside the pumping system (MPa)	410
Water orifice diameter (mm)	0.25
Focusing tube length(mm)	76.2
Focusing tube diameter (mm)	1.06
Impact angle	0^0
Abrasive material type	Australian garnet
abrasive flow rate (g/min)	120/180/240
Abrasive material average grain size	0.270 mm (80 mesh)

To clarify the variation in the erosion profile, the first-order derivative is further analyzed by numerical extraction of the kerf profile:

$$\frac{\partial h}{\partial d_w} = -\frac{d_w \cdot e^{-\frac{d_w^2}{2w^2}}}{w^2} \cdot \frac{28}{\sqrt{2}\pi^2} \cdot \frac{m_a \cdot C}{\rho_\mathrm{p} \cdot \mu \cdot \frac{0.24 \cdot d_0 \cdot \sqrt{SOD}}{2 \cdot \ln 4}} \cdot \left[\frac{\sqrt{2P/\rho_w}}{\frac{3 \cdot \sigma_f \cdot R_f^{0.6}}{\rho_p}}\right]^{2.5} \cdot \alpha_t^{1.5} \tag{9}$$

With the continuous variation in the kerf geometry, the width of the kerf also varies continuously, resulting in a change in the width of the kerf, which also reflects the dissipation law of the jet energy; therefore, the effective cutting depth is obtained by the width of the kerf:

$$\frac{\partial h}{\partial d_w} > k \Rightarrow h_e \tag{10}$$

where k is the value of the slope of the kerf profile expressed as the machining energy of the jet and h_e is the cutting depth corre-

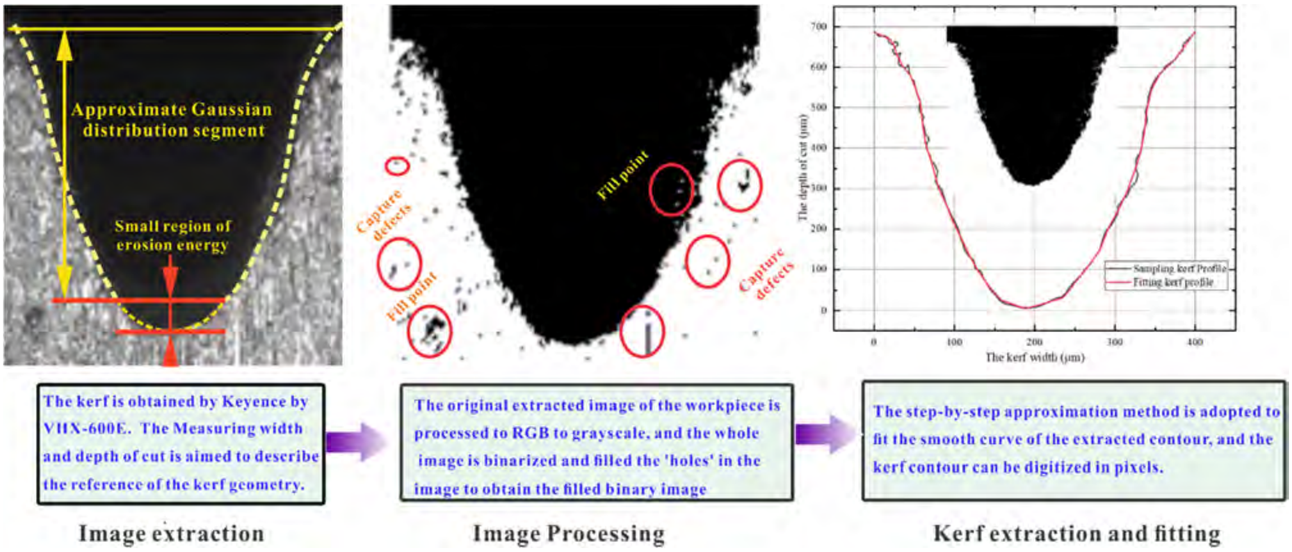

The kerf is obtained by Keyence by VHX-600E. The Measuring width and depth of cut is aimed to describe the reference of the kerf geometry.

The original extracted image of the workpiece is processed to RGB to grayscale, and the whole image is binarized and filled the 'holes' in the image to obtain the filled binary image

The step-by-step approximation method is adopted to fit the smooth curve of the extracted contour, and the kerf contour can be digitized in pixels.

Fig. 3. Image processing and kerf profile extraction.

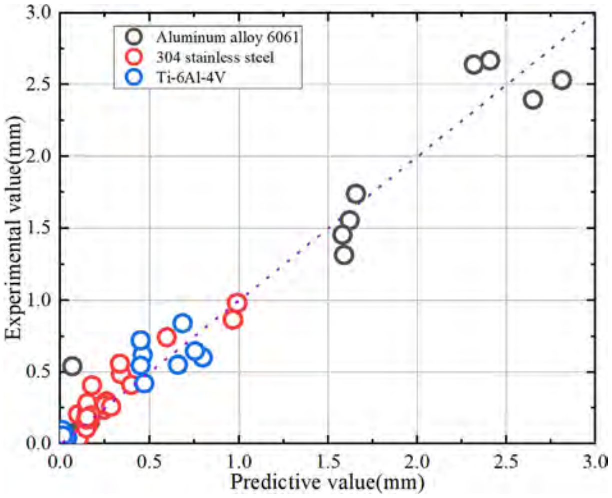

Fig. 4. Validation of the model (the predicted vs. experimental values).

sponding to when the slope of the profile is greater than k, which is also the effective cutting depth.

3. Experimental setups

3.1. Materials

Aluminum 6061 alloy, 304 stainless steel, and Ti-6Al-4 V were selected as samples for the AWJ machining experiments and were cut into samples of 200 mm × 30 mm × 15 mm. The material properties of the specimens are presented in Table 1.

3.2. Experimental procedure and analysis

The experiment was performed on an APW system an AWJ cutter, which has an output of 420 MPa using a high-pressure pump. The machining process and its detailed values are listed in Fig. 2 and Table 2, respectively.

To obtain the kerf shape, it is first necessary to extract the initial kerf profile using the VHX-600E of Keyence, as shown in Fig. 3. The

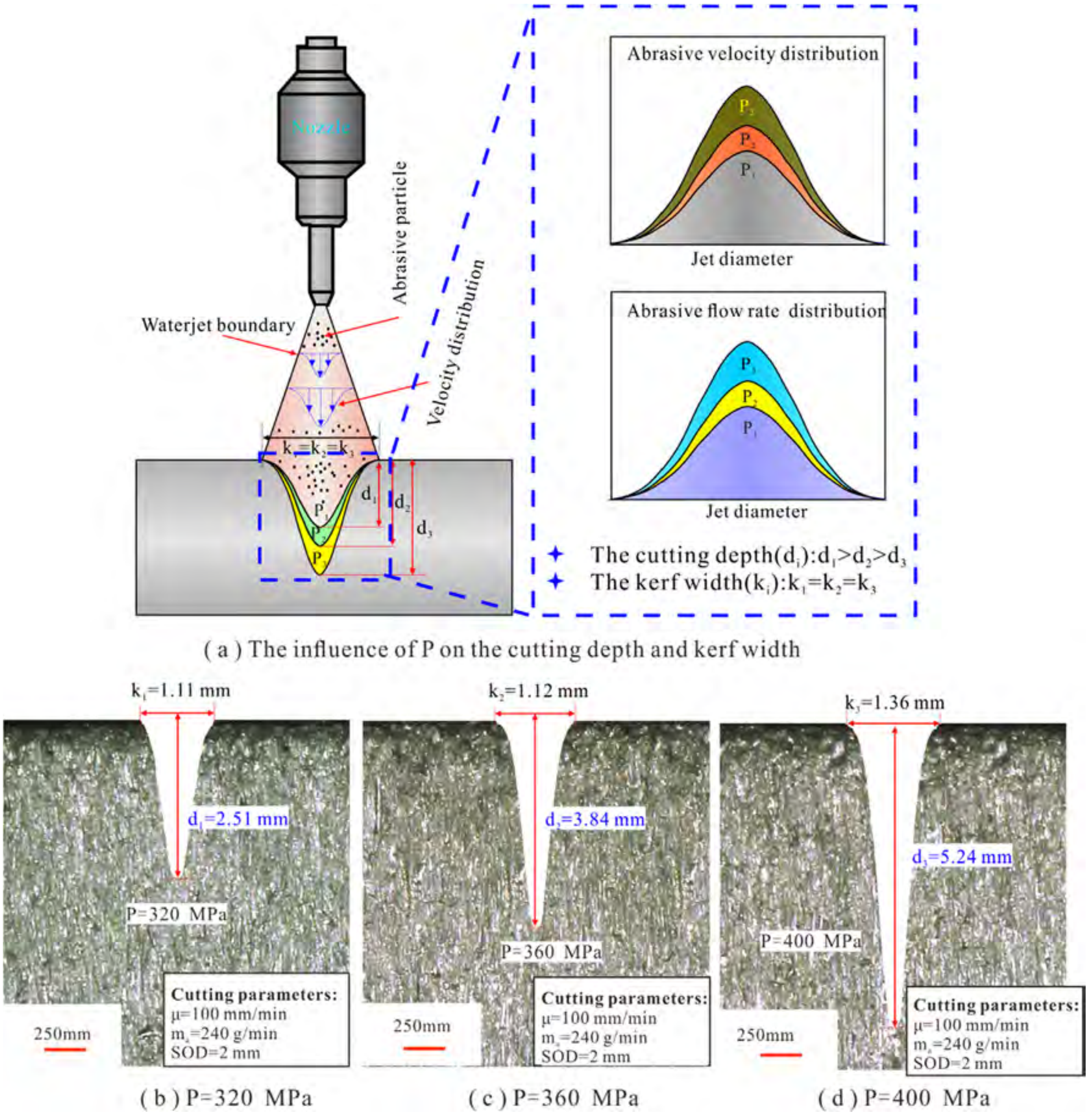

Fig. 5. Photograph of kerf cross-sectional geometry at different abrasive pressures: (a) P = 320 MPa and (b) P = 360 MPa and (c) P = 400 MPa.

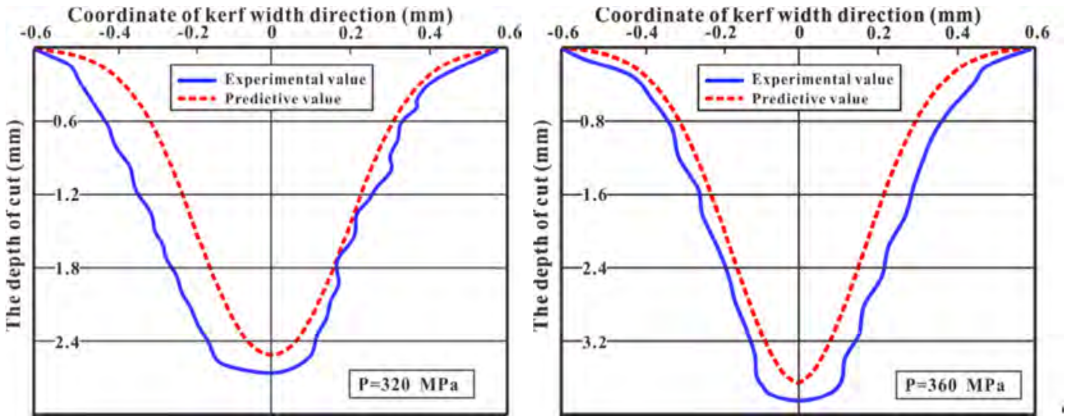

(a) P=320 MPa

(b) P=360 MPa

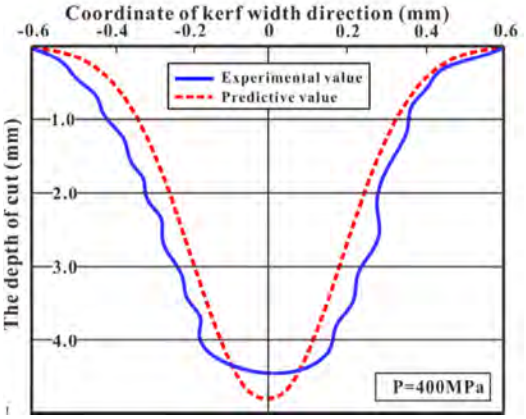

(c) P=400 MPa

Fig. 6. Comparison of experimental and predicted cut depths of kerfs at different water pressures.

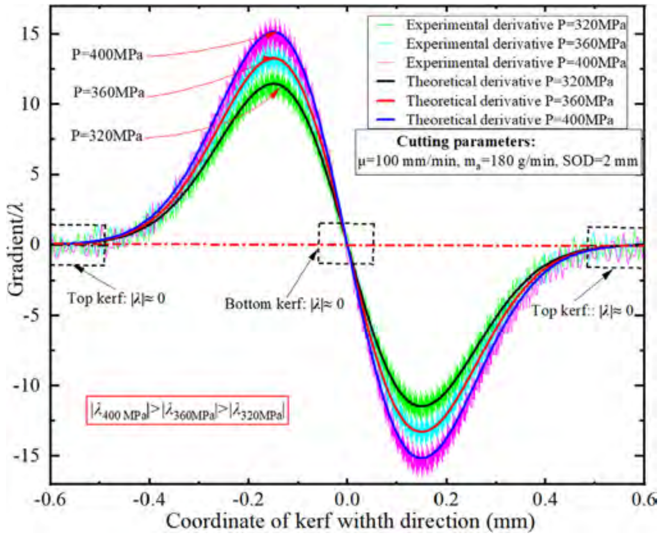

Fig. 7. Slope of kerf profile at different water pressures.

kerf image was imported into MATLAB to accurately optimize the kerf profile, including the conversion of RGB to grayscale, binarization, and image filling. Furthermore, profile fitting of the extracted contour was performed using the step-by-step approximation method, and the actual tracking and kerf profiles formed by all contour feature points obtained by step-by-step approximation were compared.

4. Result and discussion

4.1. The model verification

In this model, the effective jet diameter can be treated as the top of the kerf width, which varies according to the effective jet diameter changes owing to different standoff distances (SODs). In [31,32], the threshold velocities for the aluminum 6061 alloy, 304 stainless steel and Ti6Al4V were 90, 75, and 45 m/s respectively. It was also observed that the material flow strength and elastic modulus in the model showed a positive correlation compared to the analytical and experimental values. Additionally, the flow modulus was four times lower than the elastic modulus. Furthermore, to evaluate the abrasive particle removal process, it was observed that the grinding process particles followed a predefined trajectory for material removal, which mainly included processes such as micro-cutting and plowing [33]. The erosion removal of material during AWJ erosion is theoretically similar to the particle removal process during grinding. However, the velocity of abrasive particles in AWJ was free-flowing, and better [34]. Very little heat was generated during the ablation. Therefore, the energy required for particle removal of material in AWJ can be assumed to be the minimum energy of particles in grinding processing, and this model analysis adopts 13.6, 10.5, and 4.5 J •mm^3 for the three materials, respectively.

In Fig. 4, the correlation coefficients between the experimental and predicted values for the aluminum 6061 alloy, 304 stainless steel, and Ti6Al4V are 96.43, 99.12, and 97.53%, respectively, which

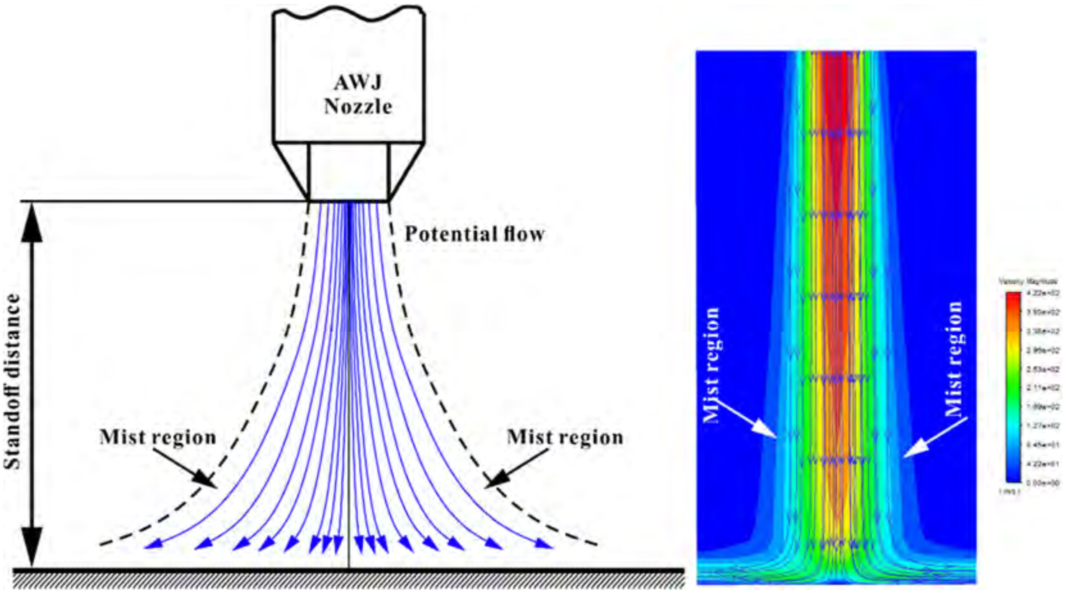

Fig. 8. Misting effect of jet energy.

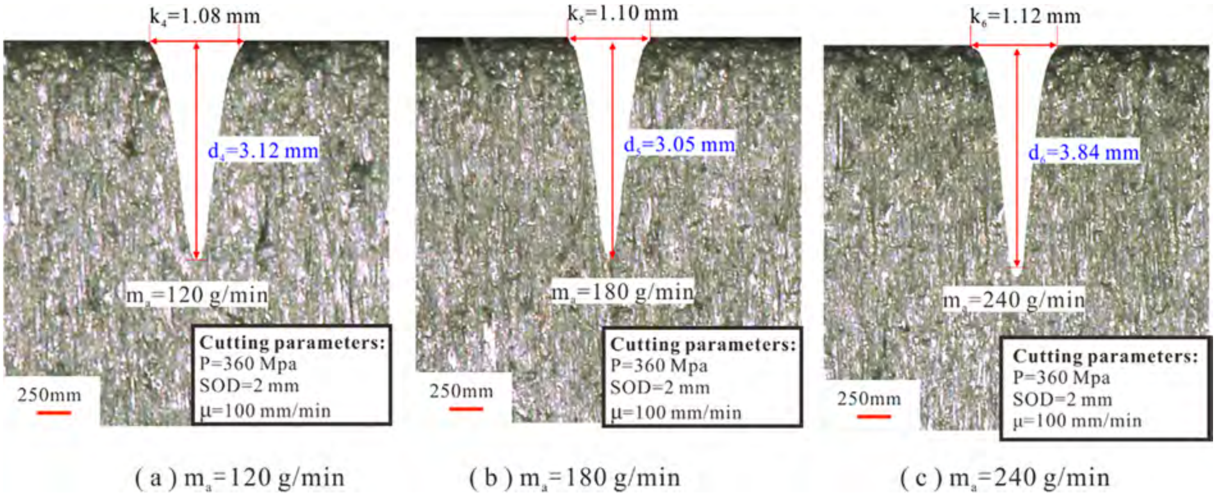

(a) m_a=120 g/min (b) m_a=180 g/min (c) m_a=240 g/min

Fig. 9. The photograph of kerf cross-sectional geometry at different abrasive flow rate: (a) ma = 120 g/min and (b) ma = 180 g/min and (c) ma = 240 g/min.

are high compared with the predictive model and experimental results.

4.2. Analysis of the jet energy distribution

Although the previous cutting depth models also consider different variations in the kerf geometry, they are also variations in linear profiles [35,36]. A more comprehensive model for the cutting depth can be developed by assuming a more consistent model of the variation in the kerf and jet energy. Furthermore, To study the effect of the variation in the jet energy on kerf profiles under different process parameters, the 2D geometry of kerf was used for the experimental analysis.

Fig. 5 shows the kerf profiles based on different water pressures. From the profile analysis of a kerf with different water pressures, it can be observed that the profile is approximated as a Gaussian distribution. As the water pressure increases, the kerf geometry does not increase uniformly along the erosion depth, and the erosion width gradually decreases. First, the disintegration of abrasive particles inside the mixing chamber and the focusing tube affected the size and distribution of abrasive particles, thus weakening the kinetic energy of the abrasive particles and reducing the erosion energy of the abrasive water jet [37,38]. Additionally, jet divergence decreased the erosion angle along the external edge of the jet plume. However, a larger erosion angle was observed closer to the jet axis, indicating higher erosion energy. A smaller erosion angle could be found far from the eroding axis; The opposite was true for erosion energy. As shown in Fig. 6, the experimental cutting depths at various water pressures coincided well with the predicted values.

In the jet erosion process, the jet energy distribution depends on the AWJ machine and cutting depth. In this study, the first-

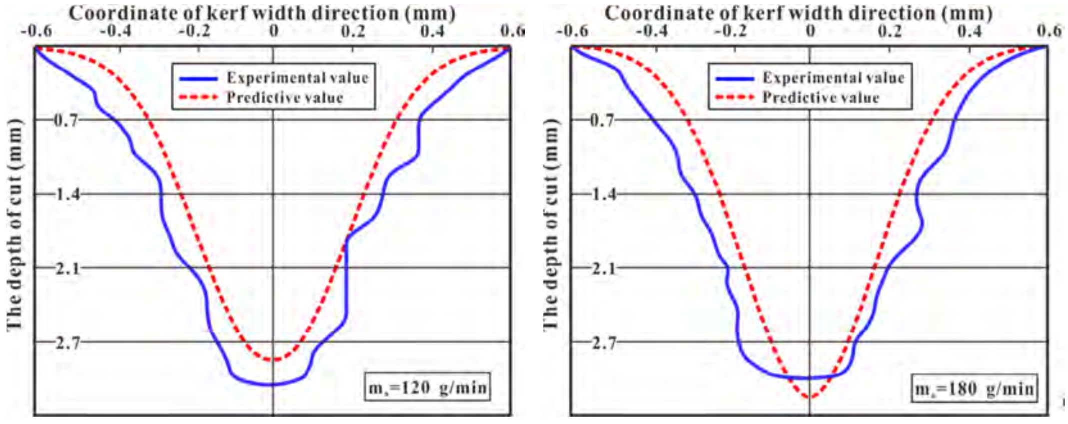

(a) m_a=120g/min (b) m_a=180g/min

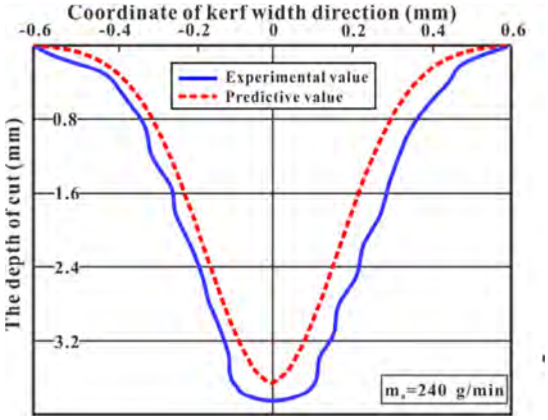

(c) m_a=240 g/min

Fig. 10. Comparison of experimental and predicted kerfs at different abrasive flow rate.

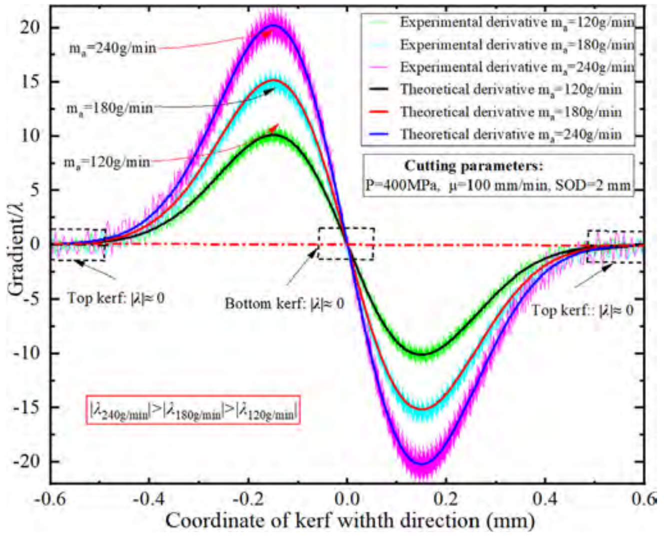

Fig. 11. Slope of kerf profile at different abrasive flow rate.

order derivative of the kerf profile was used to analyze the variation in jet energy, as shown in Fig. 7. The slope of the kerf is minimum at both the top and bottom kerf, and the slope of the kerf profile starts to increase and then decreases at the erosion range from the top edge of the kerf profile to the bottom of the profile. The jet interacts with air, resulting in the consumption of jet energy. When the jet erosion process is formed in the plane along the radial direction of the jet, the greater the contact area between the jet and air away from the axis, thus causing the jet velocity at the outer edge to be much lower than that in the core region of the jet, as shown in Fig. 8.

Additionally, the abrasive particles at the jet boundary have a low erosion capacity, and owing to their interaction with air, cannot produce significant erosion energy. In the central area of the jet, the abrasive erosion angle is almost perpendicular to the workpiece surface and there is no loss of velocity in the jet. Therefore, the abrasive interaction in the core area enhances the erosion capacity of the jet and increases the slope of the kerf profile. At the erosion boundary of the jet, the erosion angle increases with cutting depth, and the erosion slope decreases. As the cutting depth increases, the erosion energy gradually decreases. Thus, the energy distribution in the core area of the jet is gradually transferred to the outer edge of the jet, thus affecting the gradual reduction in the erosion angle of the abrasive and cutting depth owing to the jet dispersion effect.

Furthermore, the variation in jet energy in both the top and bottom with increasing water pressure was negligible based on the first-order deviation of the kerf profile. In the region between the top and bottom of the kerf, the slope of the kerf increases with increasing water pressure, as shown in Fig. 7. Therefore, as the water pressure increases, it causes an increase in jet energy and erosion capacity, leading to an increase in the rising slope of the kerf. This is because the increasing water pressure aids in the erosion rate during the erosion of abrasive particles. Therefore, the slope of the kerf profile increases with increasing water pressure.

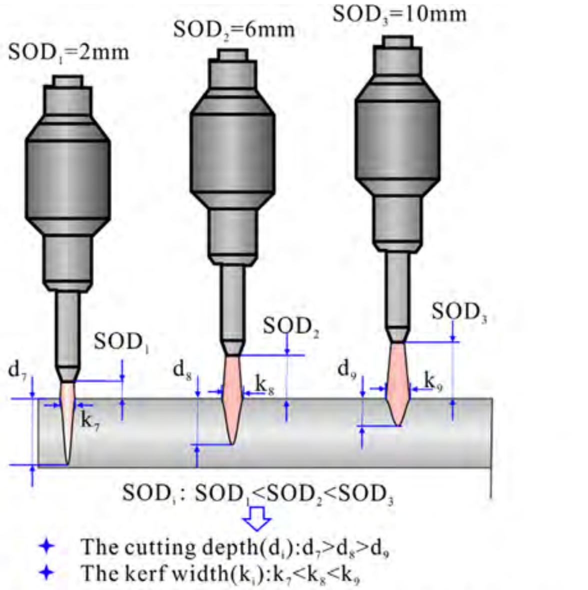

(a) The influence of SOD on the cutting depth and kerf width

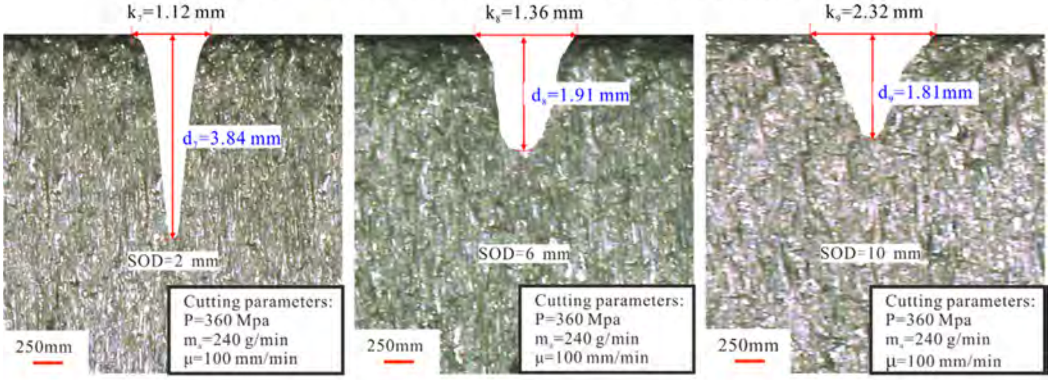

(b) SOD=2 mm (c) SOD=6 mm (d) SOD=10 mm

Fig. 12. The photograph of kerf cross-sectional geometry at different SOD: (a) SOD = 2 mm and (b) SOD = 6 mm and (c) SOD = 10 mm.

Fig. 9 shows the different kerf cross-sectional geometries along the jet axis at various abrasive flow rates in the range of 120–240 g/min. From the extracted kerf profile, it is clear that the kerf at the bottom tends to be flat and gradually shrinks into a "pocket type" owing to the decreasing jet energy with increasing cutting depth. Fig. 10 shows the kerf profile obtained by a single-factor experiment at different abrasive flow rates. The experimental cutting depths at various abrasive flow rates were in good agreement with the predicted values. As can be seen from Fig. 10, the effect of the variation in abrasive flow rate on the variation in the geometric profile of the kerf depends on the various water pressures. An explanation is provided in Fig. 11, which shows a schematic of the kerf profile slope at various abrasive flow rates. The slopes of both the top and bottom kerf widths are close to 0. The slope increases at higher abrasive flow rates, which can be attributed to variations in the erosion angle of the axial travel distance for the particle at the focusing tube tip and the radial particles in the jet column.

Fig. 12 shows the experimental results of different kerf profiles obtained at different SODs. Fig. 13 shows a comparison between the predicted and experimental profiles. As expected, the variation in the SOD produces variations in the cutting depth and kerf width. The experimental cutting depths at various SODs agree with the predicted values. The various kerf widths can be attributed to the comprehensive impact of: (i) the non-uniform distribution of jet energy, which produced a non-uniform kerf shape, resulting in a variation in the local erosion angle by single abrasive; and (ii) jet divergence owing to the change in the SOD. The kerf formation at various SODs is shown in Fig. 14. The slope has symmetric and violent fluctuations at both ends of the kerf and a large range of peak values. As the SOD increases, the slope of the kerf decreases.

As shown in Figs. 15 and 16, the cutting depth decreases with increasing focusing tube traverse speed. However, different focusing tube traverse speeds result in different kerf geometries. This may be attributable to the variation in the slope owing to the variation in the focusing tube traverse speed. In addition, the major influence of the focus tube traverse speed on the machining process is the determination of the exposure time the number of particles eroding per unit time per unit area.

The relation of the kerf width and cutting depth displays that the absolute value of the slope in first-order derivatives increases and then reduces when the cutting depth increases. The slope of the kerf profile is close to 0 in the segment of the kerf at the bottom section and the top edge, indicating that the lower the slope of the kerf profile, the lower is the cutting ability. Based on the above analysis, the slope of the kerf profile can be used to optimize the cutting depth. Therefore, the predictive model for the cutting depth adopts the aforementioned guideli-

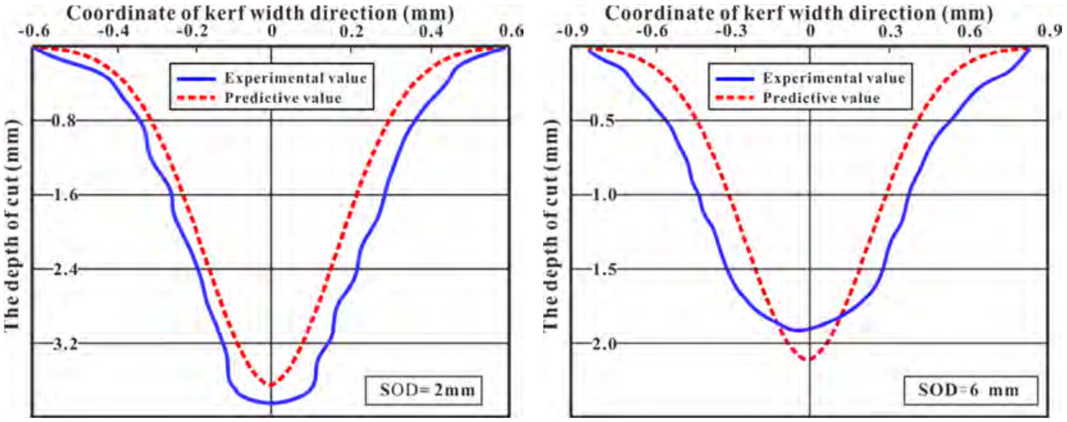

(a) SOD=2mm (b) SOD=6mm

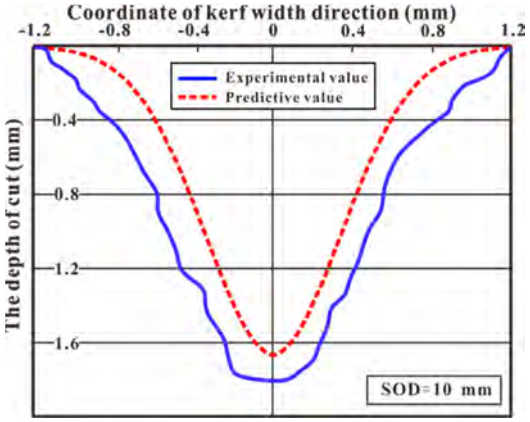

(c) SOD=10mm

Fig. 13. Comparison of experimental and predicted kerfs at different standoff distance.

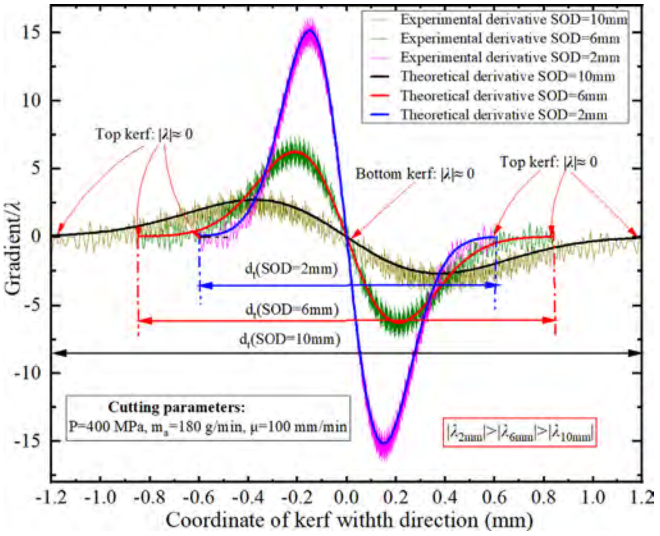

Fig. 14. Slope of kerf profile at different standoff distance.

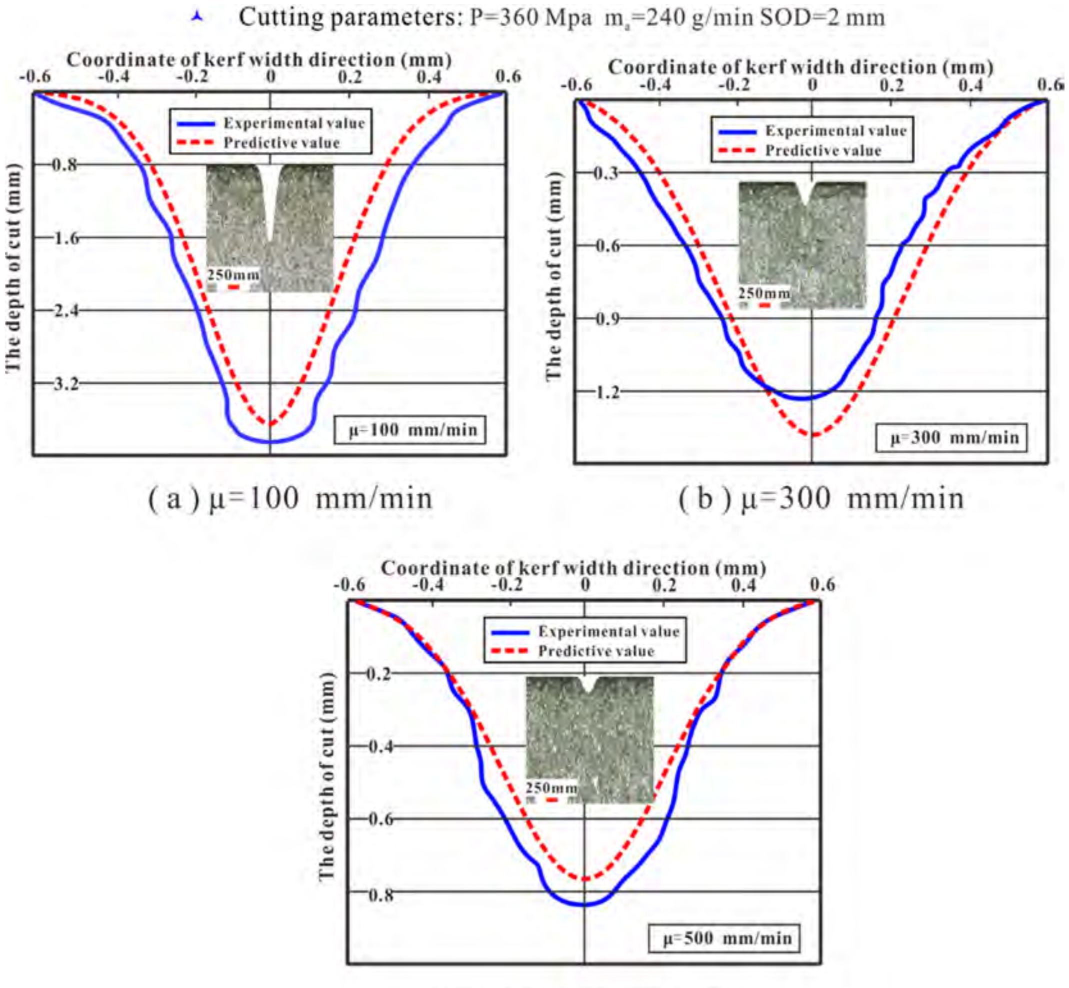

(a) μ=100 mm/min

(b) μ=300 mm/min

(c) μ=500 mm/min

Fig. 15. Comparison of experimental and predicted kerfs at different focusing tube traverse speed: (a) μ = 100 mm/min and (b) μ = 300 mm/min and (c) μ = 500 mm/min.

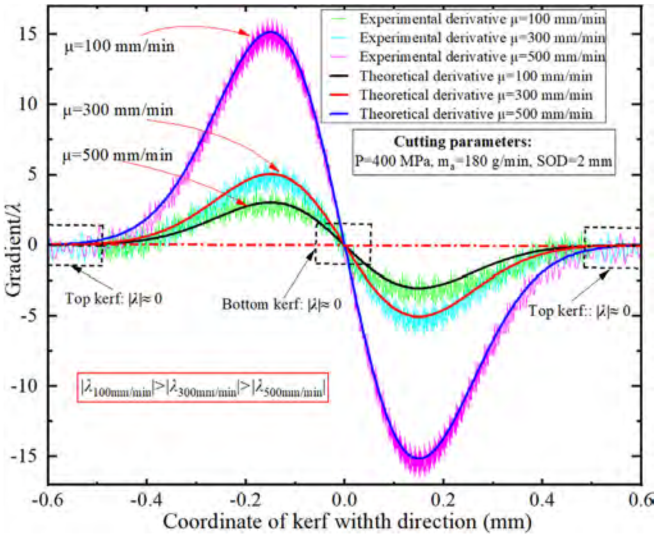

Fig. 16. Slope of kerf profile at different focusing tube traverse speed.

nes for practical AWJ machining to predict the cutting depth at fixed process parameters.

5. Conclusion

This study proposes a mathematical model of cutting depth based on the ductile material erosion process, in which the jet energy distribution follows a Gaussian function. This analytical model analyzes the change in kerf width following the cutting depth through micro-cutting and plastic deformation, which is explained using a Gaussian distribution. In addition, first-order partial derivatives of the profile prediction model of the cutting depth and kerf width were performed to analyze the distribution of jet energy and its jet decline process. The study is summarized as follows:

(1) Kerf profiles, such as binarization and image filling, are characterized by digital image processing and statistical analysis of their surface morphology. The extracted profiles were profile-fitted using a stepwise approximation. The stepwise approximation of the kerf profiles strongly corresponds to the predicted profiles.

(2) Combined with the Gaussian distribution of the jet cutting depth and width, the mathematical model calculates variations in the erosion angle and jet energy at different cutting depths during micromachining. The correlation coefficients between the experimental and predicted values of the aluminum 6061 alloy, 304 stainless steel, and Ti6Al4V are 0.9643, 0.9912, and 0.9753, respectively, which shows that the predicted value is highly correlated with the experimental value.

(3) Based on the first-order partial derivatives of the kerf profile, it is clear that the slopes of the kerf profile vary at different profile widths. At the kerf top edge and bottom, the slope of the profile is the smallest and close to zero, whereas at the kerf top edge and bottom, the slope of the profile increases and then decreases, which verifies that the energy of the jet plume is the lowest at the edge and bottom of the kerf, whereas the energy is the highest within the kerf profiles.

CRediT authorship contribution statement

Jianfeng Chen: Writing – original draft, Conceptualization, Data curation, Formal analysis, Investigation. **Yemin Yuan:** Supervision, Funding acquisition, Writing – review & editing. **Hang Gao:** Resources, Writing – review & editing. **Tianyi Zhou:** Writing – review & editing.

Data availability

No data was used for the research described in the article.

Declaration of Competing Interest

The authors declare that they have no known competing financial interests or personal relationships that could have appeared to influence the work reported in this paper.

Acknowledgments

This work is supported by NSFC-Liaoning Joint Fund (Grant No. U1908232), and Fundamental Research Funds for the Central Universities (Grant No. DUT201GF206).

We would like to thank Elsevier Language Editing Services (https://order.webshop.elsevier.com/languageservices/languageediting/.) for English language editing.

References

[1] Z. Wang, Z. Liao, Y. Yang, X. Dong, G. Augustinavicius, T. Yu, J. Zhao, Modelling and experimental study of surface treatment in abrasive waterjet peening of Nickel-based superalloy: Inverse problem, Mater. Des. 215 (2022), https://doi.org/10.1016/j.matdes.2022.110471 110471.

[2] Y. Zhang, D. Liu, W. Zhang, H. Zhu, C. Huang, Hole characteristics and surface damage formation mechanisms of C /SiC composites machined by abrasive waterjet, Ceram. Int. 48 (2022) 5488–5498, https://doi.org/10.1016/j.ceramint.2021.11.093.

[3] Z. Wang, Z. Liao, D. Axinte, X. Dong, D. Xu, G. Augustinavicius, Analytical model for predicting residual stresses in abrasive waterjet peening, Mater. Des. 212 (2021), https://doi.org/10.1016/j.matdes.2021.110209 110209.

[4] A.A. Abdel-Rahman, A.A. El-Domiaty, Maximum depth of cut for ceramics using abrasive waterjet technique, Wear. 218 (1998) 216–222, https://doi.org/10.1016/S0043-1648(98)00204-X.

[5] L. Huang, J. Folkes, P. Kinnell, P.H. Shipway, Mechanisms of damage initiation in a titanium alloy subjected to water droplet impact during ultra-high pressure plain waterjet erosion, J. Mater. Process. Technol. 212 (2012) 1906–1915, https://doi.org/10.1016/j.jmatprotec.2012.04.013.

[6] S. Paul, A. Hoogstrate, C. van Luttervelt, H.J. Kals, Analytical and experimental modelling of the abrasive water jet cutting of ductile materials, J. Mater. Process. Technol. 73 (1998) 189–199, https://doi.org/10.1016/S0924-0136(97)00228-8.

[7] V. Mohankumar, M. Kanthababu, Semi-empirical model for depth of cut in abrasive waterjet machining of metal matrix composites, J. Brazilian Soc. Mech. Sci. Eng. 42 (2020) 507, https://doi.org/10.1007/s40430-020-02581-2.

[8] C.A. Niranjan, S. Srinivas, M. Ramachandra, An Experimental Study on Depth of Cut of AZ91 Magnesium Alloy in Abrasive Water Jet Cutting, Mater. Today Proc. 5 (2018) 2884–2890, https://doi.org/10.1016/j.matpr.2018.01.082.

[9] K. Verma, V. Anandakrishnan, S. Sathish, Modelling and analysis of abrasive water jet machining of AA2014 alloy with Al2O3 abrasive using fuzzy logic, Mater. Today Proc. 21 (2020) 652–657, https://doi.org/10.1016/j.matpr.2019.06.733.

[10] Y. Ozcelik, I.C. Engin, Development of Cuttability Abacuses in Abrasive Waterjet Cutting With Regard to Depth of Cut and Roughness of Cut Surfaces, J. Test. Eval. 45 (2017), https://doi.org/10.1520/JTE20160366.

[11] G. Aydin, I. Karakurt, K. Aydiner, An experimental study on abrasive waterjet machining through design of experiment, 10th Int. Multidiscip. Sci. Geoconf. (2010) 365–371.

[12] B.S. Nie, M. Zhang, J.Q. Meng, H. Wang, R.M. Zhang, Characteristic Analysis of Metal Trough Faces Cut by Pre-mixed Abrasive Waterjet, Adv. Res. Mech. Eng. Ind. Manuf. Eng. PTS 1 2. 63–64 (2011) 740–744. https://doi.org/10.4028/www.scientific.net/AMM.63-64.740.

[13] N. Yuvaraj, M.P. Kumar, Study and evaluation of abrasive water jet cutting performance on AA5083-H32 aluminum alloy by varying the jet impingement angles with different abrasive mesh sizes, Mach. Sci. Technol. 21 (2017) 385–415, https://doi.org/10.1080/10910344.2017.1283958.

[14] G. Aydin, I. Karakurt, K. Aydiner, Prediction of the Cut Depth of Granitic Rocks Machined by Abrasive Waterjet (AWJ), Rock Mech. Rock Eng. 46 (2013) 1223–1235, https://doi.org/10.1007/s00603-012-0307-1.

[15] E. Uhlmann, H. Kruggel-Emden, C. Männel, E. Barth, D. Markauskas, Advances in Modeling of the Kerf Formation considering the Primary and Deflection Jets for the Abrasive Water Jet Technology, Procedia CIRP. 102 (2021) 156–161, https://doi.org/10.1016/j.procir.2021.09.027.

[17] J. Valíček, M. Harničárová, A. Panda, I. Hlavatý, M. Kušnerová, H. Tozan, M. Yagimli, V. Vaclavik, Mechanism of creating the topography of an abrasive water jet cut surface, in: Mach. Join. Modif. Adv. Mater., Springer, 2016: pp. 111–120.

[18] S. Paul, A.M. Hoogstrate, C.A. Van Luttervelt, H.J.J. Kals, An experimental investigation of rectangular pocket milling with abrasive water jet, J. Mater. Process. Technol. 73 (1998) 179–188, https://doi.org/10.1016/S0924-0136(97)00227-6.

[19] L.M. Hlaváč, Investigation of the abrasive water jet trajectory curvature inside the kerf, J. Mater. Process. Technol. 209 (2009) 4154–4161, https://doi.org/10.1016/j.jmatprotec.2008.10.009.

[20] D.S. Srinivasu, D.A. Axinte, P.H. Shipway, J. Folkes, Influence of kinematic operating parameters on kerf geometry in abrasive waterjet machining of silicon carbide ceramics, Int. J. Mach. Tools Manuf. 49 (2009) 1077–1088, https://doi.org/10.1016/j.ijmachtools.2009.07.007.

[21] L.M. Hlaváč, B. Strnadel, J. Kaličinský, L. Gembalová, The model of product distortion in AWJ cutting, Int. J. Adv. Manuf. Technol. 62 (2012) 157–166, https://doi.org/10.1007/s00170-011-3788-2.

[22] L.M. Hlaváč, B. Strnadel, J. Kaličinský, L. Gembalová, Investigation of the taper of kerfs cut in steels by AWJ, Int. J. Adv. Manuf. Technol. 62 (2012) 157–166, https://doi.org/10.1007/s00170-014-6578-9.

[23] A. Alberdi, A. Rivero, L.N. López de Lacalle, I. Etxeberria, A. Suárez, Effect of process parameter on the kerf geometry in abrasive water jet milling, Int. J. Adv. Manuf. Technol. 51 (2010) 467–480.

[24] L.M. Hlaváč, I.M. Hlaváčová, V. Mádr, Quick method for determination of the velocity profile of the axial symmetrical supersonic liquid jet, in, Proc. 10th Conf. Am. Waterjet WJTA. St. Louis, Missouri (1999) 189–199.

[25] J. Wang, Predictive depth of jet penetration models for abrasive waterjet cutting of alumina ceramics, Int. J. Mech. Sci. 49 (2007) 306–316, https://doi.org/10.1016/j.ijmecsci.2006.09.005.

[26] M. Hashish, Visualization of the abrasive-waterjet cutting process, Exp. Mech. 28 (1988) 159–169.

[27] D. Liu, T. Nguyen, J. Wang, C. Huang, Mechanisms of enhancing the machining performance in micro abrasive waterjet drilling of hard and brittle materials by vibration assistance, Int. J. Mach. Tools Manuf. 151 (2020), https://doi.org/10.1016/j.ijmachtools.2020.103528 103528.

[28] D. Yao, S. Pu, M. Li, Y. Guan, Y. Duan, Parameter identification method of the semi-coupled fracture model for 6061 aluminium alloy sheet based on machine learning assistance, Int. J. Solids Struct. (2022). 10.1016/j.ijsolstr.2022.111823 111823.

[29] M.A. Jalaluddin, A.A. Seman, T.K. Abdullah, Z. Hussain, Effect of aluminium and alumina ratio of aluminide coating on 304 stainless steel by slurry aluminizing, Mater, Today Proc, 2022. 10.1016/j.matpr.2022.06.528.

[30] X. Liao, Z. Liu, R. Liu, D. Mu, Microstructure evolution and joining strength of diamond brazed on Ti-6Al-4V substrates using Ti-free eutectic Ag-Cu filler alloy, Diam. Relat. Mater. 127 (2022). 10.1016/j.diamond.2022.109198 109198.

[31] D.H. Ahmed, J. Naser, R.T. Deam, Particles impact characteristics on cutting surface during the abrasive water jet machining: Numerical study, J. Mater. Process. Technol. 232 (2016) 116–130, https://doi.org/10.1016/j.jmatprotec.2016.01.032.

[32] J. Zeng, T.J. Kim, An erosion model of polycrystalline ceramics in abrasive waterjet cutting, Wear. 193 (1996) 207–217, https://doi.org/10.1016/0043-1648(95)06721-3.

[33] Z.L. Chen, B. Xiao, B. Wang, Optimum and arrangement technology of abrasive topography for brazed diamond grinding disc, Int. J. Refract. Metals Hard Mater. 95 (2021), https://doi.org/10.1016/j.ijrmhm.2020.105455.

[34] J.M. Llanto, A. Vafadar, M. Aamir, M. Tolouei-Rad, Analysis and Optimization of Process Parameters in Abrasive Waterjet Contour Cutting of AISI 304L, Metals (Basel). 11 (2021) 1362, https://doi.org/10.3390/met11091362.

[35] A.B. Guillerna, D. Axinte, J. Billingham, The linear inverse problem in energy beam processing with an application to abrasive waterjet machining, Int. J. Mach. TOOLS Manuf. 99 (2015) 34–42, https://doi.org/10.1016/j.ijmachtools.2015.09.006.

[36] A. Rabani, J. Madariaga, C. Bouvier, D. Axinte, An approach for using iterative learning for controlling the jet penetration depth in abrasive waterjet milling, J. Manuf. Process. 22 (2016) 99–107, https://doi.org/10.1016/j.jmapro.2016.01.014.

[37] L.M. Hlaváč, I.M. Hlaváčová, P. Jandačka, J. Zegzulka, J. Viliamsová, J. Vašek, V. Mádr, Comminution of material particles by water jets — Influence of the inner shape of the mixing chamber, Int. J. Miner. Process. 95 (2010) 25–29, https://doi.org/10.1016/j.minpro.2010.03.003.

[38] L.M. Hlaváč, I. Hlaváčová, J. Vašek, Milling of materials by water jets - Acting of liquid jet in the cutting head, Trans. VŠB - Tech. Univ. Ostrava, Mech. Ser. (2007) 73–84.

Further reading

[16] Y.X. Feng, C.Z. Huang, X.J. Liu, B.Q. He, The Depth Model for Abrasive Waterjet Milling of Ceramic Materials, Adv. Mater. Res. 500 (2012) 242–248, https://doi.org/10.4028/www.scientific.net/AMR.500.242.